

Contents lists available at ScienceDirect

# Acta Materialia

journal homepage: www.elsevier.com/locate/actamat





# Stress sensitivity origin of extended defects production under coupled irradiation and mechanical loading

Miao He <sup>a</sup>, Yang Yang <sup>b</sup>, Fei Gao <sup>c</sup>, Yue Fan <sup>a,\*</sup>

- <sup>a</sup> Department of Mechanical Engineering, University of Michigan, Ann Arbor, MI 48109
- <sup>b</sup> Department of Engineering Science and Mechanics, Pennsylvania State University, University Park, PA 16802
- <sup>c</sup> Department of Nuclear Engineering & Radiological Sciences, University of Michigan, Ann Arbor, MI 48109

#### ABSTRACT

The production of extended and mechanically highly consequential defects are investigated under concurrent driving forces of irradiation and stress. By using two-temperature model to account for realistic exchange of energy between the electronic subsystem and the atomic subsystem during cascades, and by controlling mechanical loading in the principal stress space to remove the dependance on a specific coordinate system, we build stress sensitivity maps for various types of irradiated dislocations. Frank loops are discovered to be dictated by volumetric strains, while Shockley partials are sensitive to volume-conserving shear loads. By tracking the microstructural evolutions during coupled irradiation and external loading, and by scrutinizing the temporal-spatial variation of local von Mises stresses near the center-collision region, the underlying mechanisms responsible for those different responses/sensitivities are elucidated. The implications of these findings in regard to a new strategy to control microstructural defects and materials performance are also discussed.

### 1. Introduction

Understanding microstructural development in materials under coupled aggressive environmental conditions is of crucial importance. For example, the next generation of nuclear reactors – a key role in the future low-carbon clean energy landscape - requires that materials can withstand for longer lifetime while being exposed to more extremes of particles flux (i.e. irradiation), stress, chemistry, temperature, etc. [1-3]. Over the past few decades, tremendous progresses have been made in uncovering the critical degradation modes caused by irradiation (e.g. swelling, embrittlement, hardening, etc.) [4-11]. In spite of these advances, the production of irradiated defects and their subsequent microstructural evolutions in the presence of multiple concurrent driving forces are way more complex and remain far less understood. For example, it is observed [12,13] that the same materials perform very differently under in-reactor environments, where they are exposed simultaneously to irradiation and external stress, as compared to post-irradiation test, where the two driving forces are applied separately. The dearth of a mechanistic understanding on materials' performance under coupled extremes is mainly due to the scarcity of available experiments, since it is very challenging to precisely control multiple drivers in real irradiation measurements and to conduct the relevant data acquisition in a time effective manner. As a result, most existing models are developed based on post-irradiation studies or theoretical hypotheses, and there is hence a pressing need to obtain a fundamental understanding and predictive capability for the microstructural development under combined driving forces [14].

In this work, we restrict our scope to the defects production in alloys under coupled irradiation and external stress. Because, as the very initial stage in the multiscale microstructural evolution, defects generation plays a critical role in shaping the system's overall microstructural development and concomitant properties changes. During high-energy collision cascades both small defects (e.g. vacancies, interstitials, and their small clusters) and extended defects (e.g. various types of dislocation loops) can be generated [10,15-19]. Here in the present study, we focus on the latter for the following two considerations: (1) Compared with point defects generation [20,21], the knowledge on the production of extended defects in the condition of coupled irradiation and stress, to the best of our knowledge, remains almost entirely blank; (2) Compared with small defects clusters, dislocations can cause more direct and profound impact to material's deformation [22-24] and other functionalities [25], and they are thus more consequential to system's overall performance.

By systematically imposing different stress states amid displacement cascade simulations – from in-plane tension/compression to pure shear and arbitrary mixtures – we scrutinize the variations of the two most populated extended defects created by irradiation, the faulted Frank loops, and the Shockley partials, respectively. We discover that their

E-mail address: fanyue@umich.edu (Y. Fan).

<sup>\*</sup> Corresponding author.

M. He et al. Acta Materialia 248 (2023) 118758

formation mechanisms, as well as their sensitivities to stresses, are remarkably different. The nucleation of Frank loop is found to be dictated by the formation energy of plate-shape interstitials cluster, which is volumetric strain sensitive. As a result, the density of irradiated Frank loops is unaffected by shear stress but exhibits strong dependence on normal stress in an asymmetrical manner: boosted under tension and suppressed under compression. In contrast, the nucleation of Shockley partial is modulated by the von Mises stress gradient and its relaxing rate near the interface between the center region of collision cascades and the matrix. The slower its relaxation, the higher chance dislocation partials can be formed and sustained. As a result, the density of irradiated Shockley partials is significantly boosted under shear stress than under normal stress. Since various types of defects play different roles in materials' microstructural evolution and their concomitant properties changes, our findings in the present study may thus enable a new way to design alloys, namely, to strategically combine irradiation and mechanical loading parameters to manipulate desired defects and hence to achieve desired performance of materials.

#### 2. Materials and methods

The defects generation induced by primary knock-on atom (PKA) are investigated through molecular dynamics simulations. To realistically capture the energy evolution during displacement cascades, in particular the electronic-atomic subsystems energy exchange, here we employ the two-temperature model (TTM) to account for the energy dissipation in the electronic subsystem, the electron-phonon coupling, and the electronic stopping effect [26–28]. More specifically, the system's heat diffusion is described by:

$$C_{e}\frac{\partial T_{e}}{\partial t} = \nabla(k_{e}\nabla T_{e}) - g_{p}(T_{e} - T_{a}) + g_{s}T_{a}$$
(1)

where  $k_e$  and  $C_e$  are the electronic thermal conductivity and the heat capacity, respectively. The right two terms represent the energy source terms due to electron-lattice exchange (with coefficient  $g_p$ ) and electron stopping (with constant  $g_s$ ), respectively.  $T_e$  and  $T_a$  are the temperatures for electronic and atomic subsystems, respectively, while  $T_a'$  represents the kinetic energy-equivalent temperature of those atoms involved into the electronic stopping process – namely the atoms with velocity higher than a critical value  $v_e$ . The two coupling constants can be expressed as:

$$g_p = \frac{3Nk_B\gamma_p}{\Delta Vm.} \tag{2}$$

$$g_s = \frac{3N^s k_B \gamma_s}{\Delta V m_i} \tag{3}$$

where  $N^s$  represents the number of the subset atoms mentioned above involved in the electronic stopping, and  $m_i$  represents atom mass.  $\gamma_p$  and  $\gamma_s$  are friction terms due to electron-phonon coupling and electronic stopping, respectively, which are related to their corresponding relaxation timescales  $\tau_p$  and  $\tau_s$ , respectively:

$$\tau_p = \frac{m_i}{\gamma_-} \tag{4}$$

$$\tau_s = \frac{m_i}{\gamma} \tag{5}$$

In this study  $\tau_s$  is taken as 0.6 ps [26], while  $g_p$  is chosen as 1.68  $\times$   $10^{18}$  Wm<sup>-3</sup>K<sup>-1</sup>, which corresponds to the value at electronic temperature of 300 K [29,30]. The electron thermal conductivity  $k_e$  is given as 21.0 Wm<sup>-1</sup>K<sup>-1</sup> [31]. The heat capacity of electron, which is a function of  $T_e$ , is calculated by the expression below using the density of states information [29,30]:

$$C_{e} = C_{0} + (a_{0} + a_{1}\widehat{T}_{e} + a_{2}\widehat{T}_{e}^{2} + a_{3}\widehat{T}_{e}^{3} + a_{4}\widehat{T}_{e}^{4})\exp(-(A\widehat{T}_{e})^{2}) \quad (\widehat{T}_{e} = T_{e} / 1000)$$
(6)

The parameters  $C_0$ ,  $a_0$ ,  $a_1$ ,  $a_2$ ,  $a_3$ ,  $a_4$ , and A are fitted as  $1.65 \times 10^{-4}$  eV/K/electron,  $-1.62 \times 10^{-4}$  eV/K/electron,  $1.94 \times 10^{-5}$  eV/K<sup>2</sup>/electron,  $-1.81 \times 10^{-6}$  eV/K<sup>3</sup>/electron,  $6.24 \times 10^{-8}$  eV/K<sup>4</sup>/electron,  $-1.06 \times 10^{-9}$  eV/K<sup>5</sup>/electron, and  $4.76 \times 10^{-2}$  K<sup>-1</sup>, respectively.

#### 3. Results and discussions

# 3.1. Coupling of irradiation and mechanical loading in principal stress space

Here we consider a NiFe-based alloy model, not only because computationally there are reliable interatomic potentials [32], but also because experimentally high-quality single crystals can be synthesized for such a system [10,33], which would ease the future validations of the hereby-obtained key modeling results and insights. To systematically examine how external stresses couple with irradiation, here we control two principal stresses in the plane normal to PKA's incident direction (e. g. Fig. 1.a), while keeping all other parameters the same (e.g. sample size, crystallography, PKA energy, chemical composition, etc.). By independently changing/combining the two principal stresses, all scenarios of stress environments -shear, normal, or mixed states - can be covered (illustrated in Fig. 1.b) without relying on a specific coordinate system, which allows one to quantitatively map out the variations of different types of irradiated defects under various stress states. And to restrain our focus on the stress-irradiation coupling, the main results in this work are for a conventional alloy Ni<sub>80</sub>Fe<sub>20</sub> at random solid solution state, while the more complex chemical/compositional effects (e.g. local chemical orders, clustering/segregations, or high-entropy effects, etc.) will be rendered to a separate study in the future. The simulation box is with dimension of  $40 \times 40 \times 40 \text{ nm}^3$  with periodic boundary conditions applied, consisting of 5.8 million atoms. Prior to irradiation, the system is first equilibrated under isothermal-isobaric ensemble at 300 K and prescribed principal stresses ( $\sigma_1$ ,  $\sigma_2$ ) in x-y plane. The collision cascade is triggered by a PKA with 50 keV kinetic energy, and as noted above in Section 2 the displacement cascades are modeled using TTM simulation. Upon irradiation, NVE ensemble is applied to the lattice subsystem with adaptive time stepping between  $10^{-7}$ – $10^{-3}$  ps, to avoid the particles being travelled by too long distance during collision cascades (in particular in the very early stage). A Langevin thermostat at room temperature is applied on a layer of the computational box boundaries with 1 nm thickness, to mimic the energy dissipation from the collision center to the bulk [26]. To reduce statistical errors, at each prescribed stress condition 10 independent simulations are performed.

# 3.2. Production of extended defects and their stress sensitivity maps

Fig. 1.c shows a typical microstructural evolution during collision cascades under an imposed stress ( $\sigma_1 = 2$  GPa,  $\sigma_2 = -3$  GPa). Note that, as shown in Supplemental Materials, such a stress level is still well located in elastic regime for the same single crystal model. In addition to the production of simple defects such as interstitials, vacancies, and/or their clusters, various types of extended defects are also generated under irradiation at different stages. The displacement cascade reaches its peak at around 1 ps, when Shockley partials 1/6112 start to nucleate at the interface between the liquid region near collision center and the solid region in the bulk. The liquid region is solidified after about 5 ps, since when other types of extended defects start to form, including Frank loop 1/3111, stair-rod dislocation 1/6110, perfect dislocation 1/2110, and Hirth dislocation 1/3100. There are no significant microstructural changes after 20 ps in simulations, and we allow the system to further

M. He et al. Acta Materialia 248 (2023) 118758

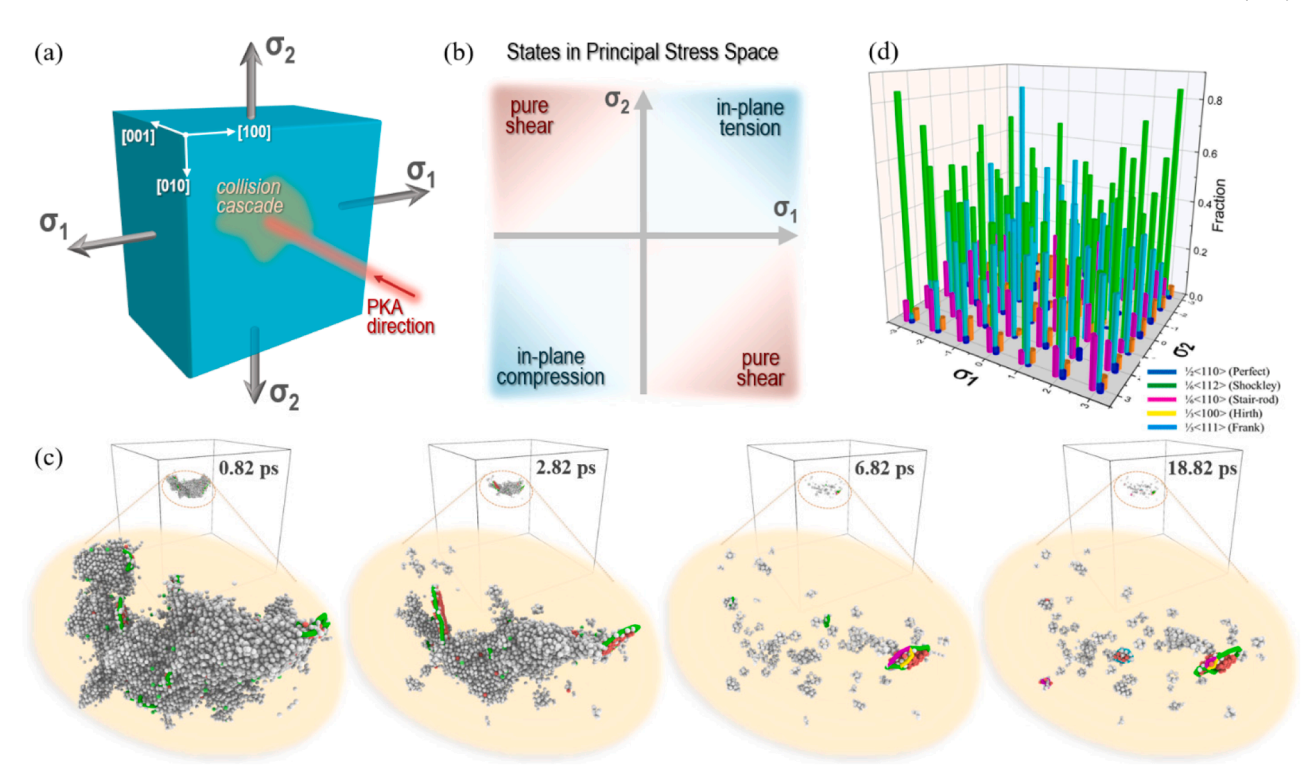


Fig. 1. Design of coupled irradiation-stress simulations and typical results. (a) Schematics of cascade simulations under controlled principal stresses of  $\sigma_1$  and  $\sigma_2$ . (b) Various stress environments in  $\sigma_1$ - $\sigma_2$  space. (c) A typical cascades simulation under  $\sigma_1$ =2 GPa and  $\sigma_2$ =-3 GPa. Atoms in red color represent HCP environments, while gray-colored atoms belong to liquid phase or other defective environments. Perfect dislocations, Shockley partials, Stair-rods, Hirth dislocations, and Frank loops are colored dark blue, green, pink, yellow, and light blue, respectively. (d) Fractions of different types of defects in principal stress space. (For interpretation of the references to colour in this figure legend, the reader is referred to the web version of this article.)

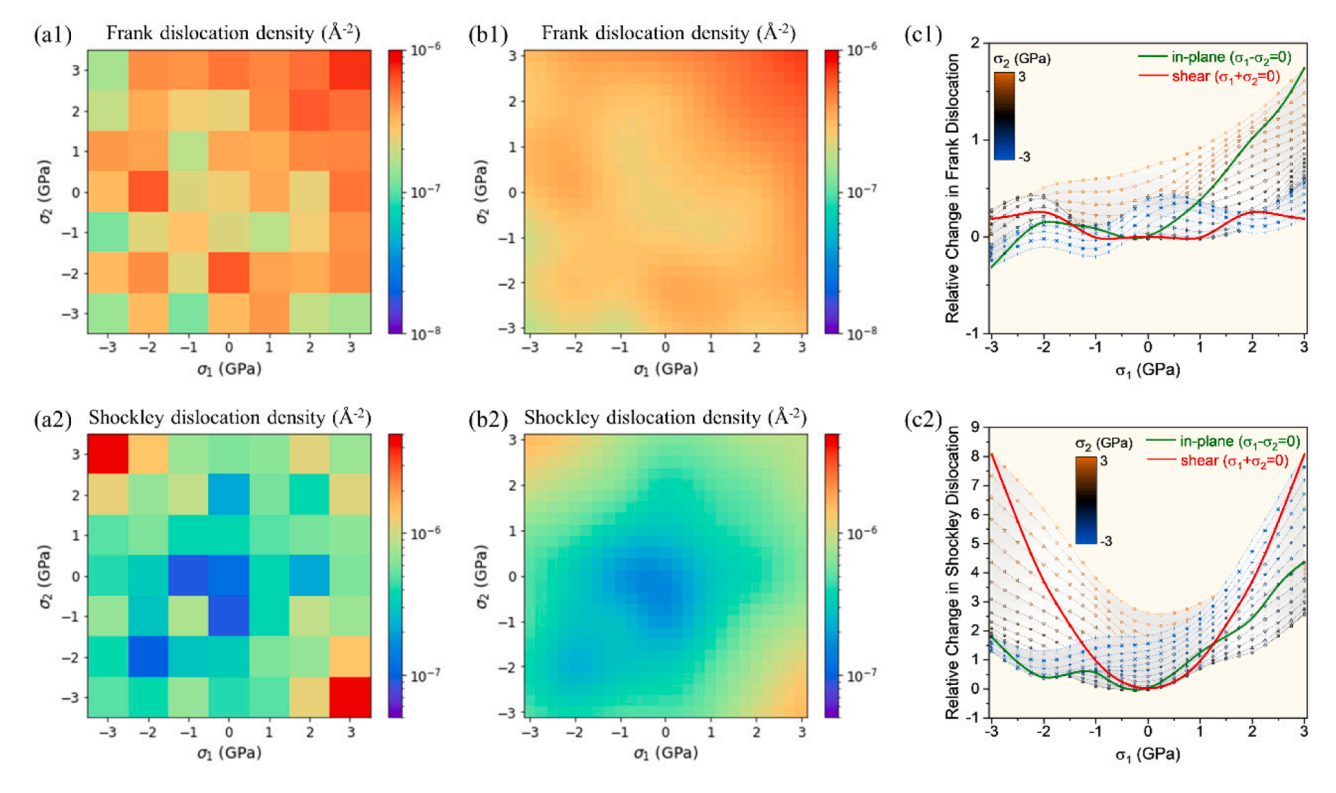


Fig. 2. Contrast of stress sensitivities on the production of Frank and Shockley dislocations. (a) Raw data on the variations of Frank loops and Shockley partials in principal stress space. (b) Refined pixel maps after TPS processing. (c) Relative changes in densities of (c1) Frank dislocations and (c2) Shockley partials at different principal stresses.

evolve for another 10 ps before we quantify the fractions of various types of defects at 30 ps. As shown in Fig. 1.d, while the fractions of different types of defects vary at different stress conditions, Shockley partials and Frank loops are the two dominant ones, which together contribute to more than 80% of total extended defects with dislocation features. We therefore restrain our scope below to these two types of extended defects.

Fig. 2.a1 and a2 show the variations of defect densities in the principal stress space for Frank loops, and Shockley partials, respectively. It is evident that both types of defects exhibit strong sensitivities to the applied global stresses, although their quantitative dependence patterns are remarkably different. For example, the production of Frank loops is enhanced near the top-right corner (i.e. in-plane tension); while the Shockley partials are proliferated near top-left and bottom-right corners (i.e. pure shear environments). Given the expensive computational costs, the interval in the principal stress space is selected as 1 GPa, and thus noticeable pixel-to-pixel fluctuations exist due to the stochastic nature of high-energy cascades. To mitigate the statistical noises, we employ thin plate spline (TPS) algorithm (details in Supplemental Materials) to interpolate the raw data in Fig. 2.a into more refined pixel maps in Fig. 2.b, based on which a more quantitative analysis can be conducted. Fig. 2.c shows the relative changes of irradiated defects densities at different stresses, defined as  $\Delta \equiv \left[\rho_D(\sigma_1, \sigma_2) - \rho_D(0, 0)\right]/\rho_D(0, \sigma_2)$ 0). Each thin line with markers represents a horizontal scan of Fig. 2.b at a controlled  $\sigma_2$ , while thick lines represent special loadings under certain constraints. More specifically, red lines correspond to the pure shear loading scenario with  $\sigma_1 + \sigma_2 = 0$ , and green lines correspond to the inplane tension/compression with  $\sigma_1 - \sigma_2 = 0$ . The production of Frank loops is observed to be suppressed under compression, promoted under tension, and almost unaffected under shear. In stark contrast, the production of Shockley partials is mostly sensitive to shear loading. These results indicate very different formation mechanisms for the two types of defects, which are discussed below.

## 3.3. Frank loops production mechanism and stress sensitivity origin

Fig. 3.a illustrates a typical formation process of Frank loops, which consist of a bundle of parallel interstitials. We then calculate the formation energy of interstitial plate in the presence of different global stresses. More specifically, we first prepare a reference system – a pristine single crystal  $Ni_{80}Fe_{20}$  alloy at random solid solution state, which is then subjected to energy minimization at controlled principal stress ( $\sigma_1$ ,

 $\sigma_2$ ). Then a (111)-oriented hexagonal plate consisting of 19 atoms is inserted into the single crystal reference system to artificially create an interstitial loop. The size of so-inserted cluster is chosen according to the average size of Frank loops observed in the irradiation simulations. A new energy minimization is then performed again to obtain the energy of the defective system,  $E_{ref+a{\rm Ni}+b{\rm Fe}}$ . Here a and b denote the numbers of inserted Ni and Fe atoms, respectively, which is set as a=15 and b=4 to keep the consistency in Ni $_{80}$ Fe $_{20}$  composition. The formation energy of the Frank loop can thus be estimated as:

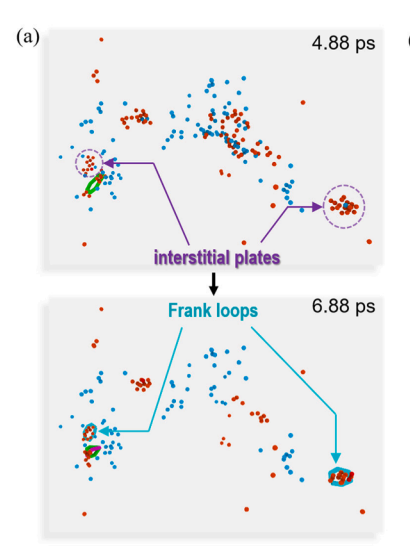
$$E^f = E_{ref+aNi+bFe} - E_{ref} - aE_{Ni} - bE_{Fe}$$
(7)

where  $E_{\text{Ni}}$  and  $E_{\text{Fe}}$  represent the average energy per Ni and Fe atom in the Ni<sub>80</sub>Fe<sub>20</sub> random solid solution reference system, respectively.

Fig. 3.b shows the so-calculated  $\it E^{f}$  under different combinations of  $\sigma_1$  and  $\sigma_2$ . The formation energy reaches its minimum/maximum under inplane tension/compression while essentially keeping invariant under pure shear. This naturally explains the key features observed in Fig. 2.c1, namely why the density of irradiated Frank loops exhibits strong dependence on normal stress in an asymmetrical manner: boosted under tension and suppressed under compression, and why its density is not significantly affected by shear stress. Admittedly, compared with the curves in Fig. 3.b, the actual variations of Frank loops density in Fig. 2.c1 exhibit finer features and are less smooth, which may be attributed to the complex local stress environments arisen from other irradiated defects nearby. Nevertheless, the overall trends in the two figures are in good agreement with each other, suggesting that formation energy of interstitials plate is the determining factor of Frank loops generation under concurrent stress and irradiation.

#### 3.4. Shockley partials production mechanism and stress sensitivity origin

In what follows we probe the formation of irradiated Shockley partial, which exhibits a qualitatively different stress sensitivity from what Frank loop does. As briefly discussed above in Fig. 1.c, Shockley partials start to form in the very early stage of collision cascades, primarily at the liquid-solid interfaces. Here we thus focus on the local stress evolution near the central collision regime. Specifically, Fig. 4.a and b map out the temporal and spatial evolution of local von Mises stress under the controlled global stresses of ( $\sigma_1=3$  GPa,  $\sigma_2=-3$  GPa), and ( $\sigma_1=3$  GPa,  $\sigma_2=3$  GPa), respectively. The local von Mises stress is defined as the averaged atomic-level shear stress within a cut-off radius of 5 Å, namely:



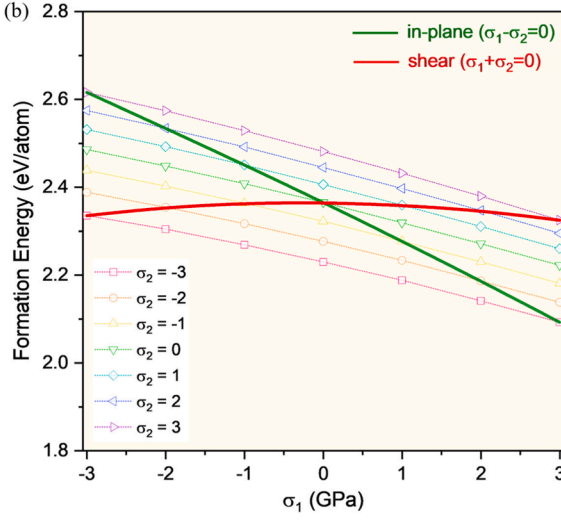


Fig. 3. Formation mechanism of Frank loops. (a) Frank loops formation in a typical cascade-induced microstructural evolution under  $\sigma_1$ =2 GPa,  $\sigma_2$ =2 GPa. Red and blue spheres represent interstitials and vacancies, respectively, using the Wigner-Seitz characterization. (b) Formation energy of an interstitial Frank loop under various combinations of  $\sigma_1$  and  $\sigma_2$ . The green and red lines correspond to in-plane tension/compression and pure shear loading, respectively. (For interpretation of the references to colour in this figure legend, the reader is referred to the web version of this article.)

M. He et al. Acta Materialia 248 (2023) 118758

$$\langle \sigma_{VM}(\overrightarrow{r}) \rangle = \sum_{|\overrightarrow{r'} - \overrightarrow{r'}| < SÅ} \sqrt{\frac{\left(\sigma_{xx}^i - \sigma_{yy}^i\right)^2 + \left(\sigma_{yy}^i - \sigma_{zz}^i\right)^2 + \left(\sigma_{zz}^i - \sigma_{xx}^i\right)^2 + 6\left(\sigma_{xy}^{i2} + \sigma_{yz}^{i2} + \sigma_{zx}^{i2}\right)}{2}} / \Omega$$
(8)

where  $\sigma^i_{a\beta}$  represents atom i's stress tensor components, and  $\Omega$  represents the total number of atoms within the local region  $\left|\overrightarrow{r}^i - \overrightarrow{r}\right| < 5\text{Å}$ .

By overlaying the Shockley partials (i.e. green segments) on the hereby-constructed local stress maps, it is clear that the nucleation of Shockley partials is most likely to occur at the location of large stress gradient, namely the interface between the liquid region near collision center and the surrounding solid region. And by comparing Fig. 4.a and b it is evident that such a formation mechanism of irradiated Shockley partials is the same, regardless of the globally imposed stress states. In spite of such consistent formation mechanism, we find the temporal and spatial evolution of  $\langle \sigma_{VM}(\overrightarrow{r}) \rangle$  significantly differ from each other under different combinations of  $\sigma_1$  and  $\sigma_2$ , which eventually lead to different densities of residual Shockley partials after irradiations. More specifically, within the first picosecond the  $\langle \sigma_{VM}(\overrightarrow{r}) \rangle$  evolutions are similar in terms of both the size of the central collision region and the local von Mises stress magnitude inside, while significant bifurcation occurs afterward. For global shear loading scenario (i.e. Fig. 4.a,  $\sigma_1 = 3$  GPa,  $\sigma_2 =$ -3 GPa), the local von Mises stress decays much slower than that in global in-plane tension scenario (i.e. Fig. 4.b,  $\sigma_1 = 3$  GPa,  $\sigma_2 = 3$  GPa). As a result, there is better chance that the nucleated Shockley partials could retain and stabilize, leading to a higher survival density in the end.

To be more quantitative, in Fig. 4.c1 and c2 we scrutinize the time evolution of irradiated Shockley partial dislocations density, and the average von Mises stress in the central collision region, respectively. As shown in Fig. 1.c, the atoms belonging to liquid phase or other defective environments form a region that the volume increases due to collision cascades and then decreases during solidification. The maximum volume varies among different systems and contains around  $5 \times 10^4$  -  $8 \times 10^4$  atoms. To illustrate the decay of the von Mises stress, we define the region with the maximum volume as the central collision region, and plot the time evolution of von Mises stress averaged over this fixed region (Fig. 4.c2). As mentioned earlier, 10 independent simulations are performed under each prescribed stress condition, and the data points in

the plots are the collection of all those independent runs. Despite the stochastic nature-induced data scatteredness, it is clear beyond standard deviations that, under the imposed global shear (red data in Fig. 4.c), the local von Mises stress can sustain at a relatively higher level after the first picosecond, which leads to a statistically higher density of survival Shockley partials. In stark contrast, in the presence of global normal loading (blue data in Fig. 4.c), the local von Mises stress decays much faster and correspondingly leads to less amount of residual Shockley partials. Such a quantitative measure is in good agreement with the structural analysis in Fig. 4.a and b, and it explains why the density of irradiated Shockley partials is significantly boosted under imposed shear loading than under normal loading.

#### 4. Conclusions

To summarize, we have utilized an extensive array of simulations to investigate the production of extended defects under the concurrent stimuli of irradiation and mechanical loading. By tuning/combining two independent principal stresses in the normal plane to PKA direction, various stress sates - ranging from pure shear to normal and mixtures are systematically implemented. Among the multiple types of defects. faulted Frank loops and Shockley partials are observed as the two most populated ones across the entire parameter space probed in the present study. However, they exhibit fundamentally different sensitivities to the applied stresses. More specifically, the concentration of irradiated Frank loops is found insensitive to shear loading ( $\sigma_1 = -\sigma_2$ ) but instead strongly dependent on normal loading in an asymmetrical manner: boosted under tension ( $\sigma_1 = \sigma_2 > 0$ ) and suppressed under compression ( $\sigma_1 = \sigma_2 < 0$ ). We further demonstrate that such a behavior of stress dependence originates from the variation pattern of formation energy of plate-shape interstitials cluster, which is volumetric strain sensitive and minimizes (maximizes) under tension (compression). Note that this is reasonable and corroborates the trend observed in earlier studies on the formation energy of small point defects (e.g. Frenkel pair) under a few

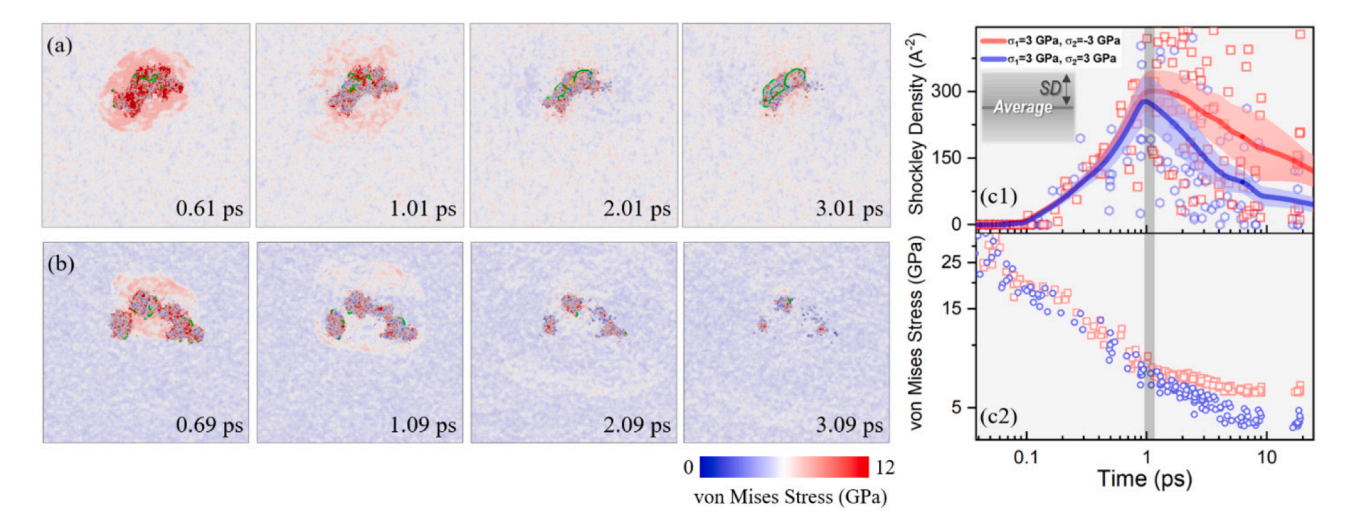


Fig. 4. Effect of external loading on local von Mises stress evolution and Shockley partial formation. Tempo-spatial evolution of local von Mises stress under controlled global (a) shear loading scenario ( $\sigma_1$ =3 GPa,  $\sigma_2$ =-3 GPa) and (b) in-plane tension scenario ( $\sigma_1$ =3 GPa,  $\sigma_2$ =3 GPa), respectively. Shockley partial dislocations are represented by green lines. (c) Time evolution of (c1) Shockley partials density and (c2) average von Mises stress in the central collision region. (For interpretation of the references to colour in this figure legend, the reader is referred to the web version of this article.)

different stress loading scenarios [21,34].

In stark contrast, the generation of Shockley partials is governed by a qualitatively different mechanism and heavily relies on the capability of maintaining a high local von Mises stress gradient near the interface between the center region of collision cascades and the matrix. In particular, in the presence of a global shear loading (i.e.  $\sigma_1 = -\sigma_2$ ), the post-cascade relaxation of local von Mises stress inside the alloy takes place at a much slower decaying rate than that under a tension/ compression loading scenario (i.e.  $\sigma_1 = \sigma_2$ ). As a result, it allows more time for the produced Shockley partials in the very early irradiation stage to stabilize and retain, which leads to a much higher density of survival Shockley partials in the top-left and bottom-right corners of Fig. 2.a2 than in other parameter space. To the best of our knowledge, this is the first time the mechanism of Shockley partials production under coupled irradiation and stress has been unveiled in a quantitative manner. To further examine the validity of this newly discovered mechanism, we consider a different alloy model with more complex chemistry, NiFeCr, a ternary alloy at equiatomic composition. As shown in Supplemental Materials (Fig. S2), a similar pattern preserves, indicating the universality of such a stress-irradiation coupling effect. On the other hand, ex/in-situ transmission electron microscopy would be helpful to further validate our prediction and offer a more comprehensive understanding in the future. Previously, diffraction contrast TEM imaging [35] and high resolution (HR) TEM [36] have been applied to image faulted dislocation loops and Shockley partials. While these methods are limited by a small field-of-view in the past, the recent development of machine learning based automatic defect classification methods [37,38] and "self-driving" [39] of TEMs may be leveraged to enable high-throughput statistical analysis over a large area.

It is worth noting that, the ability to control various types of defects is crucial to harnessing the system's mechanical properties and other functionalities. For example, recent experiments show that Shockley partials can significantly affect material's photocatalytic performance [25]. Another study on CrMnFeCoNi high-entropy alloys show that, pre-strain treatments first at low temperatures could endow the samples with much better strength-ductility synergy than being directly rendered to room-temperature mechanical tests [40]. Because the excess of nano-twins introduced in the pre-strain treatments could effectively block the motion of dislocations at later stage, causing a so-called dynamic Hall-Petch effect and thus providing more endured hardening rate. Bearing the similar spirit, we believe our key findings in the present study – the essentially opposite responses of Frank loops and Shockley partials variations to external stress loadings - may have important implications, because the two types of defects play different roles in material's mechanical performance. More specifically, as one of the most prevalent slip systems in FCC lattice, Shockley partial dislocations can serve as immediate and direct plasticity carriers. By contrast, Frank loops are more likely to shape the system's overall mechanical behaviors at a longer timescale due to its sessile nature and in an indirect manner by interacting with other dislocations to trigger twinning deformation [41,42]. Therefore, by following the guidance in Fig. 2 and strategically tuning irradiation and mechanical loading parameters, this study may offer an orthogonal route to manipulate desired defects in alloys at proper time or deformation stage, hence achieving desired materials properties.

#### **Declaration of Competing Interest**

The authors declare that they have no known competing financial interests or personal relationships that could have appeared to influence the work reported in this paper.

#### Acknowledgement

This work was funded by National Science Foundation under award DMR-1944879. Y.Y. acknowledges the support from the National

Science Foundation early career award DMR-2145455.

#### Supplementary materials

Supplementary material associated with this article can be found, in the online version, at doi:10.1016/j.actamat.2023.118758.

#### References

- R.W. Grimes, R.J. Konings, L. Edwards, Greater tolerance for nuclear materials, Nat. Mater. 7 (9) (2008) 683–685.
- [2] D.J. Hill, Nuclear energy for the future, Nat. Mater. 7 (9) (2008) 680-682.
- [3] R.W. Grimes, W.J. Nuttall, Generating the option of a two-stage nuclear renaissance, Science 329 (5993) (2010) 799–803.
- [4] C. Cawthorne, E.J. Fulton, Voids in irradiated stainless steel, Nature 216 (5115) (1967) 575–576.
- [5] R.S. Barnes, Embrittlement of stainless steels and nickel-based alloys at high temperature induced by neutron radiation, Nature 206 (4991) (1965) 1307–1310.
- [6] C. Lu, L. Niu, N. Chen, K. Jin, T. Yang, P. Xiu, Y. Zhang, F. Gao, H. Bei, S. Shi, M.-R. He, I.M. Robertson, W.J. Weber, L. Wang, Enhancing radiation tolerance by controlling defect mobility and migration pathways in multicomponent single-phase alloys, Nat. Commun. 7 (1) (2016) 13564.
- [7] G. Ackland, Controlling radiation damage, Science 327 (5973) (2010) 1587–1588.
- [8] K. Nordlund, J. Keinonen, M. Ghaly, R.S. Averback, Coherent displacement of atoms during ion irradiation, Nature 398 (6722) (1999) 49–51.
- [9] B.D. Wirth, How does radiation damage materials? Science 318 (5852) (2007) 923–924
- [10] F. Granberg, K. Nordlund, M.W. Ullah, K. Jin, C. Lu, H. Bei, L.M. Wang, F. Djurabekova, W.J. Weber, Y. Zhang, Mechanism of radiation damage reduction in equiatomic multicomponent single phase alloys, Phys. Rev. Lett. 116 (13) (2016), 135504.
- [11] A.S. Fraser, I.R. Birss, C. Cawthorne, High-temperature embrittlement of stainless steel irradiated in fast fluxes, Nature 211 (5046) (1966) 291–292.
- [12] J. Pakarinen, S. Tähtinen, B.N. Singh, A comparative TEM study of in-reactor and post-irradiation tensile tested copper, J. Nucl. Mater. 442 (1) (2013) S821–S825. Supplement 1.
- [13] B.N. Singh, H. Xiaoxu, S. Taehtinen, P. Moilamen, P. Jacquet, J. Dekeyser, Final report on in-reactor uniaxial tensile deformation of pure iron and Fe-Cr alloy, Denmark, 2007, p. 52.
- [14] C. Ji, Y. Cui, Y. Li, N. Ghoniem, A concurrent irradiation-mechanics multiscale coupling model, J. Mech. Phys. Solids 167 (2022), 105005.
- [15] X.M. Bai, A.F. Voter, R.G. Hoagland, M. Nastasi, B.P. Uberuaga, Efficient Annealing of Radiation Damage Near Grain Boundaries via Interstitial Emission, Science 327 (5973) (2010) 1631–1634.
- [16] N. Gao, Z.W. Yao, G.H. Lu, H.Q. Deng, F. Gao, Mechanisms for <100>interstitial dislocation loops to diffuse in BCC iron, Na.t Commun. 12 (1) (2021) 225.
- [17] X. Zhang, K. Hattar, Y. Chen, L. Shao, J. Li, C. Sun, K. Yu, N. Li, M.L. Taheri, H. Wang, J. Wang, M. Nastasi, Radiation damage in nanostructured materials, Prog. Mater. Sci. 96 (2018) 217–321.
- [18] H. Xu, R.E. Stoller, Y.N. Osetsky, D. Terentyev, Solving the Puzzle of \$(100)\$ Interstitial Loop Formation in bcc Iron, Phys. Rev. Lett. 110 (26) (2013), 265503.
- [19] E. Levo, F. Granberg, C. Fridlund, K. Nordlund, F. Djurabekova, Radiation damage buildup and dislocation evolution in Ni and equiatomic multicomponent Ni-based alloys, J. Nucl. Mater. 490 (2017) 323–332.
- [20] M.J. Banisalman, T. Oda, Atomistic simulation for strain effects on threshold displacement energies in refractory metals, Comput. Mater. Sci. 158 (2019) 346–352.
- [21] B. Beeler, M. Asta, P. Hosemann, N. Grønbech-Jensen, Effects of applied strain on radiation damage generation in body-centered cubic iron, J. Nucl. Mater. 459 (2015) 159–165.
- [22] G.S. Was, Fundamentals of Radiation Materials Science Metals and Alloys, Springer, Germany, 2007.
- [23] B. Wu, Z. Bai, A. Misra, Y. Fan, Atomistic mechanism and probability determination of the cutting of Guinier-Preston zones by edge dislocations in dilute Al-Cu alloys, Phys. Rev. Mater. 4 (2) (2020), 020601.
- [24] X.-.Z. Tang, Y.-.F. Guo, L. Sun, Y. Fan, S. Yip, B. Yildiz, Strain rate effect on dislocation climb mechanism via self-interstitials, Mater. Sci. Eng.: A 713 (2018) 141–145.
- [25] Z. Han, W. Hong, W. Xing, Y. Hu, Y. Zhou, C. Li, G. Chen, Shockley partial dislocation-induced self-rectified 1D hydrogen evolution photocatalyst, ACS Appl. Mater. Interfaces 11 (22) (2019) 20521–20527.
- [26] E. Zarkadoula, G. Samolyuk, W.J. Weber, Two-temperature model in molecular dynamics simulations of cascades in Ni-based alloys, J. Alloys Compd. 700 (2017) 106–112.
- [27] A.M. Rutherford, D.M. Duffy, The effect of electron-ion interactions on radiation damage simulations, J. Phys.: Condensed Matter 19 (49) (2007), 496201.
- [28] Y. Zhang, T. Egami, W.J. Weber, Dissipation of radiation energy in concentrated solid-solution alloys: unique defect properties and microstructural evolution, MRS Bull. 44 (10) (2019) 798–811.
- [29] M. He, C. Wu, M.V. Shugaev, G.D. Samolyuk, L.V. Zhigilei, Computational study of short-pulse laser-induced generation of crystal defects in Ni-based single-phase binary solid-solution alloys, J. Phys. Chem. C 123 (4) (2019) 2202–2215.

- [30] Z. Lin, L.V. Zhigilei, V. Celli, Electron-phonon coupling and electron heat capacity of metals under conditions of strong electron-phonon nonequilibrium, Phys. Rev. B 77 (7) (2008), 075133.
- [31] C.Y. Ho, M.W. Ackerman, K.Y. Wu, S.G. Oh, T.N. Havill, Thermal conductivity of ten selected binary alloy systems, J. Phys. Chem. Ref. Data 7 (3) (1978) 959–1178.
- [32] G. Bonny, N. Castin, D. Terentyev, Interatomic potential for studying ageing under irradiation in stainless steels: the FeNiCr model alloy, Modelling and Simulation in, Mater. Sci. Eng. 21 (8) (2013), 085004.
- [33] K. Jin, H. Bei, Y. Zhang, Ion irradiation induced defect evolution in Ni and Ni-based FCC equiatomic binary alloys, J. Nucl. Mater. 471 (2016) 193–199.
- [34] Q. Guo, K. Lai, Y. Tang, H. Wen, B. Wang, Effects of applied strain on defect production and clustering in FCC Ni, J. Nucl. Mater. 537 (2020), 152191.
- [35] Y.Q. Sun, P.M. Hazzledine, A TEM weak-beam study of dislocations in γ' in a deformed Ni-based superalloy, Philos. Mag. A 58 (4) (1988) 603–617.
- [36] Q. Lin, X. An, H. Liu, Q. Tang, P. Dai, X. Liao, In-situ high-resolution transmission electron microscopy investigation of grain boundary dislocation activities in a

- nanocrystalline Cr<br/>MnFeCoNi high-entropy alloy, J. Alloys Compd. 709 (2017) 802–807.
- [37] M. Shen, G. Li, D. Wu, Y. Yaguchi, J.C. Haley, K.G. Field, D. Morgan, A deep learning based automatic defect analysis framework for In-situ TEM ion irradiations, Comput. Mater. Sci. 197 (2021), 110560.
- [38] R. Sainju, W.-.Y. Chen, S. Schaefer, Q. Yang, C. Ding, M. Li, Y. Zhu, DefectTrack: a deep learning-based multi-object tracking algorithm for quantitative defect analysis of in-situ TEM videos in real-time, Sci. Rep. 12 (1) (2022) 15705.
- [39] M. Xu, A. Kumar, J. LeBeau, Automating electron microscopy through machine learning and USETEM, Microsc. Microanal. 27 (S1) (2021) 2988–2989.
- [40] G. Laplanche, A. Kostka, O.M. Horst, G. Eggeler, E.P. George, Microstructure evolution and critical stress for twinning in the CrMnFeCoNi high-entropy alloy, Acta Mater. 118 (2016) 152–163.
- [41] T. Nogaret, C. Robertson, D. Rodney, Atomic-scale plasticity in the presence of Frank loops, Philos. Mag. 87 (6) (2007) 945–966.
- [42] M. Niewczas, G. Saada, Twinning nucleation in Cu-8 at.% Al single crystals, Philos. Mag. A 82 (1) (2002) 167–191.